Complete crystal-field calculation of Zeeman hyperfine splittings in europium

Kieran M. Smith [1], Michael F. Reid [2,3] Matthew J. Sellars,[1] and Rose L. Ahlefeldt[1]

[1]*Centre for Quantum Computation and Communication Technology, Research School of Physics,
The Australian National University, Canberra, Australia*
[2]*School of Physical and Chemical Sciences, University of Canterbury, PB 4800, Christchurch 8041, New Zealand*
[3]*Dodd-Walls Centre for Photonic and Quantum Technologies, New Zealand*

Computational crystal-field models have provided consistent models of both electronic and Zeeman-hyperfine structure for several rare-earth ions. However, a computational crystal-field calculation of Eu^{3+} incorporating the lattice electric quadrupole and nuclear Zeeman interactions has not been performed. Here, we include these terms in a computational model to fit the crystal-field levels and the Zeeman-hyperfine structure of the $^7F_0$ and $^5D_0$ states in three Eu^{3+} sites: the C_{4v} and C_{3v} sites in CaF_2 and the C_2 site in $EuCl_3 \cdot 6H_2O$. Close fits are obtained for all three sites which are used to resolve ambiguities in previously published parameters, including quantifying the anomalously large crystal-field-induced state mixing in the C_{3v} site and determining the signs of Zeeman-hyperfine parameters in all three sites. We show that this model allows accurate prediction of properties for Eu^{3+} important for quantum information applications of these ions, such as relative transition strengths. The model could be used to improve crystal-field calculations for other non-Kramers singlet states. We also present a spin Hamiltonian formalism without the normal assumption of no J mixing, suitable for other rare-earth ion energy levels where this effect is important.

I. INTRODUCTION

Crystals containing rare-earth ions are now extensively studied for quantum information applications, particularly quantum memories. These applications almost always require precise knowledge of the hyperfine structure of the rare-earth ion in the optical ground and excited states employed. In memory protocols such as the gradient echo memory [1] or the atomic frequency comb protocol [2], hyperfine structure information is used to spectrally prepare the memory by pumping population at specific frequencies into nonresonant hyperfine states. Knowledge of the hyperfine structure is also used to predict the locations of ZEFOZ (zero first order Zeeman) [3] points where hyperfine transitions are protected from dephasing caused by magnetic fluctuations, and to identify fields at which Λ transitions with favorable oscillator strengths for quantum memories can be obtained [4,5].

Hyperfine structure is typically determined from experimental data recorded over a range of magnetic fields, which is then fitted to a spin Hamiltonian that parameterizes any electronic contributions to the nuclear structure. This approach has been used very successfully, for instance, for predicting ZEFOZ points in $Eu^{3+}:Y_2SiO_5$ to extend the coherence time by six orders of magnitude [6]. However, there are both limitations and drawbacks to using spin Hamiltonians. They cannot be applied when the electronic contributions to the nuclear structure are not constant, for instance, for Kramers rare-earth ions over a large range of magnetic fields. The experimental data can also contain many lines, particularly for ions with high nuclear spin or in crystals with multiple magnetic subsites, which can be difficult to fit to a spin Hamiltonian, especially in the case of low symmetry where there are many

free parameters. Finally, the spin Hamiltonian often provides little physical insight into the ion or the site.

An alternative is to use a full crystal-field model for the whole $4f$ configuration of the rare-earth ion, including interactions that generate hyperfine structure. These types of models have been successfully applied for several different hosts doped with Kramers and non-Kramers rare-earth ions, including Pr^{3+} [5,7–10], Er^{3+} [11–14], Ho^{3+} [7,15–21], Tb^{3+} [22,23], and Tm^{3+} [4,10]. However, a complete crystal-field calculation of Eu^{3+} Zeeman-hyperfine structure has not been demonstrated. Terms that are omitted from computational crystal-field calculations of other ions due to their relatively small contributions become important in the commonly studied $J = 0$ crystal-field levels in Eu^{3+}. These are the electric quadrupole contribution from the lattice field gradient, and the nuclear Zeeman. The qualitative contribution of these terms to the Zeeman-hyperfine structure in Eu^{3+} is well-established [24–27], but accurate estimates of their exact size in different sites have largely been lacking. Here, we implement a crystal-field model with all contributions included, and apply the model to three different Eu^{3+} sites: the C_{4v} and C_{3v} sites in CaF_2, and the C_2 site in $EuCl_3 \cdot 6H_2O$. We also extract spin Hamiltonian parameters from the crystal-field fit and discuss how crystal-field models can be used to resolve ambiguities in the spin Hamiltonian.

II. THEORETICAL BACKGROUND

A. crystal-field Hamiltonian

Here, we first present the full crystal-field Hamiltonian for the $4f$ configuration with expressions for each individual

term. Most of these expressions have been covered in detail, [4,5,28–30], but here we give all terms in a unified notation.

The complete Hamiltonian appropriate for modeling the $4f^N$ configuration is

$$H = H_{\mathrm{FI}} + H_{\mathrm{CF}} + H_{\mathrm{Z}} + H_{\mathrm{HFS}}. \tag{1}$$

The terms in Eq. (1) represent the free-ion, crystal-field, electronic and nuclear Zeeman, and hyperfine interactions, respectively. Note we have grouped terms of comparable magnitude, however, the hyperfine interactions also generate splittings in the free-ion and can be considered to be free-ion interactions.

The free-ion Hamiltonian H_{FI} (excluding the hyperfine interactions) can be expressed as [31]

$$H_{\mathrm{FI}} = E_{\mathrm{avg}} + \sum_{k=2,4,6} F^k f_k + \zeta_{4f} A_{\mathrm{SO}} + \alpha L(L+1)$$
$$+ \beta G(G_2) + \gamma G(R_7) + \sum_{i=2,3,4,6,7,8} T^i t_i$$
$$+ \sum_{i=0,2,4} M^i m_i + \sum_{i=2,4,6} P^i p_i. \tag{2}$$

In this equation, E_{avg} describes the spherically symmetric part of the Hamiltonian which shifts the entire configuration, F^k and ζ_{4f} describe the electrostatic and spin-orbit integrals, respectively, and f_k and A_{SO} represent the angular parts of the electrostatic and spin-orbit interactions, respectively. The remainder of the terms are smaller and parametrize two- [32,33] and three- [34] body interactions, as well as higher-order spin-dependent effects [35,36]. Methods for calculating matrix elements using reduced matrix elements tabulated by Nielson and Koster [37] have been covered in detail [29]. Mean free-ion parameters have been tabulated for the rare-earth ions [38], however it is necessary to allow E_{avg}, the Slater parameters F^k, and spin orbit parameter ζ_{4f} to vary during fitting to experimental levels as these parameters have the most significant effect on the calculated spectra.

The crystal-field Hamiltonian H_{CF} can be written as

$$H_{\mathrm{CF}} = \sum_{k=2,4,6} \sum_{q=-k}^{k} B_q^k C_q^{(k)}, \tag{3}$$

where B_q^k are the crystal-field expansion coefficients, and $C_q^{(k)}$ are spherical tensor operators using Wybourne's normalization of the spherical harmonics Y_{kq} [28]. The B_q^k with nonzero q may be complex in low symmetries, and in that case the real and imaginary parts must be considered as independent, real parameters. Table IV in Ref. [39] lists the nonzero parameters for each of the crystallographic point groups. We note that there are a variety of conventions in the literature for labeling the real and imaginary parts [40].

In the presence of an external magnetic field **B**, the Zeeman Hamiltonian H_{Z} is [24]

$$H_{\mathrm{Z}} = H_{eZ} + H_{nZ}, \tag{4}$$

$$\text{with} \quad H_{eZ} = \mu_B \mathbf{B} \cdot (\mathbf{L} + g_s \mathbf{S}), \tag{5}$$

$$H_{nZ} = -g_n \mu_N \mathbf{B} \cdot \mathbf{I}, \tag{6}$$

where H_{eZ} is the electronic Zeeman interaction and H_{nZ} the nuclear Zeeman interaction. **L** and **S** are the total electronic orbital and spin angular momentum operators, g_s is the electron spin g factor, μ_B is the Bohr magneton, μ_N is the nuclear magneton, and g_n is the nuclear g factor. Matrix elements for these terms are given in Refs. [4,5].

Hyperfine structure arises from the interaction of nucleus with the electronic states and with the field gradient generated by the lattice. Generally, only interactions involving the nuclear magnetic dipole moment and electric quadrupole moment are important [28]. The hyperfine Hamiltonian H_{HFS} is then expressed as

$$H_{\mathrm{HFS}} = H_{\mathrm{MD}} + H_{\mathrm{Q}}, \tag{7}$$

where H_{MD} and H_{Q} are the contributions from magnetic dipole and electric quadrupole moment interactions, respectively.

The coupling of the nuclear magnetic dipole to the orbital and spin angular momenta of the electrons results in Ref. [33]

$$H_{\mathrm{MD}} = a_l \sum_i \mathbf{N}_i \cdot \mathbf{I}, \tag{8}$$

$$\mathbf{N}_i = \mathbf{l}_i - \sqrt{10}(\mathbf{s}\mathbf{C}^{(2)})_i^{(1)}, \tag{9}$$

where $\mathbf{l_i}$ and $\mathbf{s_i}$ are the orbital and spin angular momenta of the electron i, and **I** is the nuclear spin operator.

In our calculations, a_l is treated as a free parameter. It may be estimated as [28]

$$a_l = 2\mu_B g_n \mu_N \frac{\mu_0}{4\pi}(1-R)\langle r_e^{-3} \rangle, \tag{10}$$

where μ_0 is the vacuum permeability, R is a shielding factor due to closed electron shells [25,41,42], and $\langle r_e^{-3} \rangle$ is the average inverse-cube radius of the $4f$ orbital.

The nuclear quadrupole moment couples to the $4f$ electrons and to the lattice:

$$H_{\mathrm{Q}} = H_{\mathrm{Q}}^{4f} + H_{\mathrm{Q}}^{\mathrm{lat}}. \tag{11}$$

The coupling to the $4f$ electrons may be written as [29]

$$H_{\mathrm{Q}}^{4f} = E_Q \frac{1}{2}\left(\frac{(I+1)(2I+1)(2I+3)}{I(2I-1)}\right)^{\frac{1}{2}} \mathbf{U}_n^{(2)} \cdot \mathbf{U}_e^{(2)}, \tag{12}$$

where **U** are unit tensor operators. Here $\mathbf{U}_e^{(2)}$ operates on the electronic part of the wave function and $\mathbf{U}_n^{(2)}$ operates on the nuclear part.

We treat E_Q as a free parameter, but it may be estimated from

$$E_Q = \frac{-e^2 Q}{4\pi \epsilon_0}(1-R)\langle r_e^{-3} \rangle, \tag{13}$$

where the nuclear quadrupole moment Q is introduced via

$$\langle I||r_n^2 C_n^{(2)}||I \rangle = \frac{Q}{2}\left(\frac{(I+1)(2I+1)(2I+3)}{I(2I-1)}\right)^{\frac{1}{2}}, \tag{14}$$

where r_n is the nuclear radius.

The coupling of the nucleus to the electric field gradient of the surrounding ions has the same form as the crystal-field interaction. In the following, the N_q^2 are parameters, analogous

to the B_q^2, and the unit tensor $(U_n)_q^{(2)}$ acts on the nuclear spin:

$$H_Q^{\text{lat}} = \sum_{q=-2}^{2} N_q^2 (U_n)_q^{(2)}. \qquad (15)$$

Matrix elements for the lattice and $4f$ quadrupole terms are provided in Refs. [4,5].

Since the N_q^2 and B_q^2 both parametrize interactions with the lattice, an approximate relationship between them may be derived by assuming that both may be estimated from the point-charge lattice potential [4,5], corrected by relevant shielding factors: $(1 - \gamma_\infty)$ for the nucleus, and $(1 - \sigma_2)$ for the $4f$ electrons. By including the relevant reduced matrix elements, we may write

$$N_q^2 = \frac{-(1 - \gamma_\infty)}{(1 - \sigma_2)\langle r_e^2 \rangle} \frac{Q}{2} \left(\frac{(I+1)(2I+1)(2I+3)}{I(2I-1)} \right)^{\frac{1}{2}} B_q^2. \quad (16)$$

Here, $\langle r_e^2 \rangle$ is the mean square radius of the $4f$ orbital. We do not expect this relationship to be exact, since the crystal-field interaction is far from purely electrostatic, and the shielding/antishielding factors R, γ_∞, and σ_2 do vary between materials. In our calculations N_q^2 and E_Q were free parameters in the model bounded by known ranges of the shielding/antishielding factors [43] and the ratio and signs of the B_q^2 parameters.

B. Previous modeling of Zeeman-hyperfine structure

Although most previous crystal-field modeling for rare-earth crystals has considered only H_{FI} and H_{CF}, several workers have included certain of the hyperfine and Zeeman terms. To understand when it is necessary to include the various hyperfine and Zeeman terms it is useful to examine relative sizes of the various contributions in different types of electronic states.

For the Kramers doublets in ions such as Er^{3+}, the true doublet states directly allow for a large first order magnetic dipole contribution to the hyperfine splittings, with minor effects from the electron-nuclear $4f$ quadrupole interaction. Therefore accurate fits to crystal-field levels and hyperfine structure can be achieved by incorporating only the magnetic dipole and $4f$ quadrupole contributions. Crystal-field fits have been demonstrated for Er^{3+} in several materials including $LiYF_4$ [11,12], YPO_4 [14], and both sites of Y_2SiO_5[13].

Similar to the Kramers doublets, the non-Kramers doublets and pseudodoublets are also largely dependent on the magnetic dipole interaction. In true doublets there is again a large first order magnetic dipole term. In pseudodoublet ground states (two singlets split by only a few cm^{-1}) it is the second order magnetic dipole interaction, commonly referred to as the pseudoquadrupole (see Sec. III B), that has the largest contribution. Provided the crystal-field splitting of the pseudodoublet ground state is accurately modeled, satisfactory fits to the hyperfine splittings of transitions can be achieved by calculating the magnetic dipole interaction, with the $4f$ quadrupole having only a minor effect on the splittings [15]. Hyperfine structure of non-Kramers doublets and pseudodoublets has been successfully calculated using crystal-field models in several hosts, including CaF_2

[7,8,15,23], SrF_2 [8,23], $LiYF_4$ [20,22], KY_3F_{10} [18], $CaWO_4$ [19], $YAl_3(BO_3)_4$ [16], YPO_4 [17], and both sites of Y_2SiO_5 [21].

For non-Kramers singlet states in $J \neq 0$ multiplets, the largest contribution to the hyperfine splittings can vary depending on the magnitude of the splittings to nearby crystal-field levels within the multiplet. If this splitting is large ($>100\,cm^{-1}$), the level mixing is typically too small to allow for a significant pseudoquadrupole contribution. The largest contribution is then the $4f$ quadrupole, but the lattice quadrupole may also need to be considered [5,9,10,44].

For non-Kramers singlets with $J = 0$, such as $^7F_0$ and $^5D_0$ in Eu^{3+}, the situation is quite different. H_Q^{lat} and H_{nZ} are the dominant sources of the hyperfine splittings as H_{eZ}, H_{MD} and H_Q^{4f} have zero matrix elements for $J = 0$ states. It is only through J-mixing induced by the crystal field that these terms contribute at all. In these cases, an accurate calculation of the crystal-field energies is important, as the magnitudes of the contributions are sensitive to the splittings of nearby multiplets.

For the Zeeman terms, the true nuclear Zeeman is nearly always considered unimportant as the enhancement of the nuclear moment due to the magnetic dipole (the pseudonuclear effect, see Sec. III B) is several orders of magnitude larger than the bare nuclear moment in most situations [45]. However, the true nuclear Zeeman effect becomes important in $J = 0$ multiplets, where the pseudonuclear term is small, or in cases where the crystal-field mixing results in a large pseudonuclear Zeeman component for a magnetic field applied in only one direction, such as $Tm^{3+}:Y_3Al_5O_{12}$ [4].

III. SPIN HAMILTONIAN THEORY

As described above, the first goal of this paper is to provide accurate crystal-field models for Eu^{3+} sites. The second goal, addressed in this section, is to provide a direct relationship between the crystal-field model and the phenomenological spin Hamiltonian models commonly used in experimental studies of hyperfine structure of individual crystal-field levels. The widely used existing expression [46] suitable for other non-Kramers singlet states is inappropriate for the $J = 0$ levels of Eu^{3+} because it ignores J mixing effects. A crystal-field derived expression both allows a physical interpretation of the spin Hamiltonian parameters and resolves certain parameter ambiguities that arise when fitting phenomenological models.

A. Phenomenological spin Hamiltonian

For an electronic singlet state, the appropriate phenomenological spin Hamiltonian contains operators for the nuclear spin only:

$$H_{\text{eff}} = (\mathbf{B} \cdot \mathbf{Z} \cdot \mathbf{B})\mathbf{1} + \mathbf{B} \cdot \mathbf{M} \cdot \mathbf{I} + \mathbf{I} \cdot \mathbf{Q} \cdot \mathbf{I}, \qquad (17)$$

where $\mathbf{B}$ is the magnetic field, $\mathbf{I}$ is the nuclear spin operator, $\mathbf{1}$ is the identity operator, $\mathbf{Z}$ is the quadratic Zeeman tensor, $\mathbf{M}$ the linear Zeeman tensor, and $\mathbf{Q}$ the traceless enhanced quadrupole tensor. These three symmetric tensors are unique to that electronic state, and are only constrained by the site symmetry. The most general form of these tensors (applicable

to C_1 symmetry) is

$$\mathbf{Z} = \mathbf{R}_Z \cdot \begin{bmatrix} Z_x & 0 & 0 \\ 0 & Z_y & 0 \\ 0 & 0 & Z_z \end{bmatrix} \cdot \mathbf{R}_Z^T, \tag{18}$$

$$\mathbf{M} = \mathbf{R}_M \cdot \begin{bmatrix} g_x & 0 & 0 \\ 0 & g_y & 0 \\ 0 & 0 & g_z \end{bmatrix} \cdot \mathbf{R}_M^T, \tag{19}$$

$$\mathbf{Q} = \mathbf{R}_Q \cdot \begin{bmatrix} -E - \frac{1}{3}D & 0 & 0 \\ 0 & E - \frac{1}{3}D & 0 \\ 0 & 0 & \frac{2}{3}D \end{bmatrix} \cdot \mathbf{R}_Q^T, \tag{20}$$

where $\mathbf{R}_i = R(\varphi_i, \theta_i, \psi_i)$ is an Euler rotation matrix. In C_2 symmetry, the lowest symmetry studied here, $\varphi = \theta = 0$ for all tensors when the laboratory frame z is aligned with the C_2 axis. For axial symmetries such as C_{4v} and C_{3v}, all tensors are aligned, $g_x = g_y$, and $E = 0$.

Experimentally, the spin Hamiltonian parameters required for the particular site symmetry are fit to hyperfine splitting data for a variety of magnetic field values, typically obtained using nuclear magnetic resonance, optically detected nuclear magnetic resonance, or Raman heterodyne spectroscopy. Such a fit furnishes a set of nonunique spin Hamiltonian parameters, because the spin Hamiltonian is insensitive to certain transformations. For instance, in C_2 symmetry the Hamiltonian is insensitive to the sign of $\mathbf{Z}$, $\mathbf{M}$, $\mathbf{Q}$, g_z, and D, and the sign of E is ill-defined since it can be reversed by rotating the entire spin Hamiltonian $90°$ about z.

Further, there are three possible sets of parameters corresponding to different, equivalent choices of the quantization axis of the quadrupole term. Any one set accurately fits the spin Hamiltonian of a single electronic state, but problems arise when trying to calculate parameters that depend on spin Hamiltonians of two different electronic states. For example, the relative optical transition probability P_{ij} of transitions between different hyperfine states in ground (i) and excited (j) levels calculated from the overlap of the nuclear wave functions Ψ^n as

$$P_{ij} = \left| \left\langle \Psi_{gi}^n \middle| \Psi_{ej}^n \right\rangle \right|^2, \tag{21}$$

only holds true if the same quadrupole quantization axes have been used for both spin Hamiltonians.

Further difficulty arises in materials with multiple magnetically inequivalent subsites, which occur in materials where the rare-earth site symmetry is lower than the crystal symmetry. While the spin Hamiltonian of all subsites can be generated from the spin Hamiltonian for one site using the symmetry operations of the crystal, the same base subsite must be correctly chosen for every electronic level. When there is no obvious relationship between spin Hamiltonian parameters in different electronic levels, identifying the same subsite can be very difficult [47].

Additional measurements, such as the relative optical oscillator strength measurements described above, can resolve some but not all of these ambiguities. A crystal-field-based spin Hamiltonian, in contrast, can resolve all physically significant spin Hamiltonian parameter ambiguities.

B. Crystal-field-based spin Hamiltonian

A spin Hamiltonian for a particular electronic state may be extracted from the full crystal-field Hamiltonian by projecting the crystal-field Hamiltonian into the spin Hamiltonian basis [13,48]. For a general discussion of projecting Hamiltonians into a smaller basis, see Ref. [49]. The projection approach allows the direct calculation of the $\mathbf{Z}$, $\mathbf{M}$, and $\mathbf{Q}$ parameters with all sign and rotational ambiguities removed, by comparing the projected Hamiltonian with the spin Hamiltonian matrix. It is also possible to use a perturbation-theory approach to approximate the relationship between a crystal-field calculation and the spin Hamiltonian.

The spin Hamiltonian for a non-Kramers singlet state, ignoring J mixing, is commonly written as [46,50]

$$H = -\mathbf{B} \cdot \left(g_J^2 \mu_B^2 \mathbf{\Lambda} \right) \cdot \mathbf{B} - \mathbf{B} \cdot \left(g_n \mu_N \mathbf{1} - 2A_J g_J \mu_B \mathbf{\Lambda} \right) \cdot \mathbf{I} \\ - \mathbf{I} \cdot \left(A_J^2 \mathbf{\Lambda} + \mathbf{T}_Q \right) \cdot \mathbf{I}, \tag{22}$$

where g_J is the Landé g value, and A_J is the hyperfine interaction parameter for that state. The lattice and $4f$ quadrupole contributions are combined into a single true quadrupole term $\mathbf{T_Q}$ and $A_J^2 \mathbf{\Lambda}$ accounts for the pseudoquadrupole contribution arising from the magnetic dipole interaction. The contributions from other electronic states are encapsulated by the tensor $\mathbf{\Lambda}$ which sums the interaction with all other states in the multiplet:

$$\Lambda_{ij} = \sum_{n=1}^{2J+1} \frac{\langle 0|J_i|n\rangle \langle n|J_j|0\rangle}{E_n - E_0}, \tag{23}$$

with $|0\rangle$ the singlet state of interest.

When dealing with only the hyperfine splittings, the first term of Eq. (22) is ignored. This form is sufficient when working within a single LSJ state, as the largest contributions to the splittings come from interactions with crystal-field levels within the same multiplet. Summation over the electron configurations of a single multiplet allows for many of the interactions to be related to the total angular momentum operator $\mathbf{J}$, simplifying the form of the spin Hamiltonian; $\mathbf{\Lambda}$ can be used to describe several effects that have the same symmetry despite originating from different physical interactions.

For the $J = 0$ multiplets of Eu^{3+}, the J mixing between multiplets is crucial [50]. This prevents the electron configuration summation being used to relate the hyperfine interactions to $\mathbf{J}$, hence preventing the construction of $\mathbf{\Lambda}$. Instead, we now sum over all possible electronic states $|\Psi\rangle = |\tau LSJM_J\rangle$ of the $4f^N$ configuration for which the matrix elements of $\mathbf{L} + g_s\mathbf{S}$ and $\mathbf{N}$ are nonzero.

The first correction is the pseudonuclear Zeeman. We replace $\mathbf{\Lambda}$ by

$$\alpha_{ij} = \sum_{\Psi'} \frac{\langle \Psi | L_i + g_s S_i | \Psi' \rangle \langle \Psi' | N_j | \Psi \rangle}{E_{\Psi'} - E_{\Psi}}, \tag{24}$$

where we consider the mixing of levels by the electronic Zeeman and magnetic dipole interactions. Accounting for the pseudonuclear Zeeman effect, the nuclear g values can be calculated as

$$g_i = g_n \mu_N - 2a_l g_J \mu_B \alpha_{ii} \tag{25}$$

The second correction is the pseudoquadrupole. We replace $\mathbf{\Lambda}$ by

$$P_{ij} = \sum_{\Psi'} \frac{\langle\Psi|N_i|\Psi'\rangle\langle\Psi'|N_j|\Psi\rangle}{E_{\Psi'} - E_\Psi}, \tag{26}$$

where we consider the second order contribution from the magnetic dipole interaction. The D and E associated with the pseudoquadrupole are then given by

$$D_{pq} = a_l^2 \left(\frac{P_{xx} + P_{yy}}{2} - P_{zz}\right), \tag{27}$$

$$E_{pq} = a_l^2 \frac{P_{xx} - P_{yy}}{2}. \tag{28}$$

We also separate the true quadrupole term $\mathbf{T}_Q$ into its two contributions, the lattice $\mathbf{T}_{\text{lat}}$ and $4f$ quadrupole $\mathbf{T}_{4f}$, with forms equivalent to Eq. (20). These then have D and E parameters related to the hyperfine parameters N_q^2 and E_Q by

$$D_{\text{lat}} = \frac{3N_0^2}{I(2I-1)}\left(\frac{I(2I-1)}{(I+1)(2I+1)(2I+3)}\right)^{\frac{1}{2}}, \tag{29}$$

$$E_{\text{lat}} = \sqrt{\frac{2}{3}} \frac{N_2^2}{N_0^2} D_{\text{lat}}, \tag{30}$$

for the lattice contribution, and

$$D_{4f} = \frac{3E_Q}{I(2I-1)}\left\langle\psi\left|\sum_i (C_{ei})_0^{(2)}\right|\psi\right\rangle, \tag{31}$$

$$E_{4f} = \sqrt{\frac{2}{3}} \frac{\langle\psi|\sum_i (C_{ei})_2^{(2)}|\psi\rangle}{\langle\psi|\sum_i (C_{ei})_0^{(2)}|\psi\rangle} D_{4f}, \tag{32}$$

for the $4f$ contribution. Here, $|\psi\rangle$ is the wave function for the state in question, accounting for crystal-field mixing.

The spin Hamiltonian for any J-mixing dependent system is then given by

$$\begin{aligned} H = &-\mathbf{B}\cdot(g_n\mu_N\mathbf{1} - 2a_l g_J\mu_B\boldsymbol{\alpha})\cdot\mathbf{I} \\ &-\mathbf{I}\cdot(a_l^2\mathbf{P} + \mathbf{T}_{\text{lat}} + \mathbf{T}_{4f})\cdot\mathbf{I}. \end{aligned} \tag{33}$$

Due to the J-mixing dependence of the interactions, the principal axes of the quadrupole terms of Eq. (33) are not necessarily aligned. Instead, each contribution takes the form of Eq. (20) with a unique set of D, E, and Euler angles. The contributions are summed in a common frame to form a total quadrupole tensor, with principal axes given by D_{tot} and E_{tot}, which are not necessarily aligned with the principal axes of any of the individual quadrupole terms. This is in contrast to the nuclear Zeeman tensor which has principal axes that are aligned with the pseudonuclear Zeeman contribution as the pure nuclear Zeeman is isotropic.

IV. METHOD

Crystal-field calculations were performed using M. F. Reid's F-shell empirical program suite in conjunction with S. Horvath's *pycf* program for low symmetry crystal-field parameter fitting [51]. A truncated set of matrix elements was used to reduce computation time following the approach of

Carnell *et al.*[52] by first diagonalizing the free-ion Hamiltonian Eq. (2) using estimates of the free-ion parameters [31], and then using a truncated set of eigenvectors of this diagonalization to generate free-ion and crystal-field matrix elements in the intermediate coupled basis. We chose to truncate the matrix elements at 30 free-ion multiplets out of the total 295, resulting in 272 crystal-field levels out of the total 3003, with energies up to $\sim$33 000 cm^{-1}.

For each of the Eu^{3+} centers analyzed, first the free-ion parameters E_{avg}, F^k, and ζ_{4f} along with the crystal-field parameters B_q^k required for the site symmetry were fitted to available crystal-field energy levels (see Table I in Ref. [39]). This was done to ensure a satisfactory fit to the crystal-field levels before including the hyperfine interactions as adding the nuclear spin means a sixfold increase in the number of states and in the computation time. Next, the crystal-field parameters were refitted using the previous parameters as initial values at the same time as fitting the hyperfine parameters a_l, E_Q, and N_q^2. Whilst the lattice quadrupole parameters N_q^2 have a fixed relationship to the crystal-field parameters B_q^2, theoretically requiring the addition of only a single scaling parameter to account for shielding effects, we instead used free parameter for each q term. This was done to avoid propagating error from the crystal-field parameters onto the hyperfine structure, which is discussed in Sec. VI. Instead, bounds were placed on N_q^2 such that the appropriate sign and approximate relative magnitudes were correctly imposed by the B_q^2 parameters.

For this second round of fitting, the fitting data were the crystal-field energy levels, and the hyperfine splittings of the $^7F_0$ state and the $^5D_0$ state (when available) calculated for 100 magnetic field directions defined on a spiral:

$$\mathbf{B} = \begin{bmatrix} B_0\sqrt{1-t^2}\cos(6\pi t) \\ B_0\sqrt{1-t^2}\sin(6\pi t) \\ B_0 t \end{bmatrix}, \tag{34}$$

where $B_0 = 400$ mT. We fitted to hyperfine splittings and not absolute frequencies so that any error in the energy of the crystal-field levels was not propagated into the hyperfine errors. This way, the hyperfine splittings could still be fitted even if there was a deviation of the crystal-field levels away from the experimental values.

In crystal-field theory, there always exist sets of crystal-field parameters that produce equivalent fits to energy level structure for a given site, but different wave functions and ordering of M_J levels within the multiplets. These sets do not produce the same Zeeman-hyperfine splittings, so this data is needed to constrain the crystal-field values. To avoid the fit getting stuck in a local minimum within the crystal-field parameter set two methods were employed; a basin-hopping algorithm [53,54] was used to allow the fit to jump between equivalent sets, and the weighting of the hyperfine and crystal-field levels was chosen such that both contributed approximately equally to calculated error.

The fit was accomplished using the multi-Hamiltonian method [51] where a crystal-field Hamiltonian is generated for each magnetic field step then diagonalized concurrently. In this method, the parameters can be fitted using experimental data for both the zero-field crystal-field levels and Zeeman-hyperfine splittings simultaneously.

TABLE I. Fitted crystal-field parameters (cm^{-1}) for the three Eu^{3+} sites studied here. Where a parameter is blank, that parameter does not occur for the site symmetry.

Parameter	CaF_2:C_{4v}	CaF_2:C_{3v}	$EuCl_3 \cdot 6H_2O$
E_{avg}	64154	64232	63887
F_2	83479	83317	82962
F_4	60024	59405	59580
F_6	42506	42658	42801
ζ	1333	1337	1333
B_0^2	680	2122	70
B_2^2	–	–	$241 + 196i$
B_0^4	−852	1697	−334
B_2^4	–	–	$335 + 465i$
B_3^4	–	−2095	–
B_4^4	−994	–	$-316 - 175i$
B_0^6	1317	−657	700
B_2^6	–	–	$308 - 396i$
B_3^6	–	−913	–
B_4^6	−1311	–	$727 - 432i$
B_6^6	–	1366	$-269 + 175i$
a_l	0.0405	0.0433	0.0386
E_Q	−0.0490	−0.0497	−0.0408
N_0^2	−0.00619	−0.0111	−0.000853
N_2^2	–	–	$-0.00466 - 0.00225i$

V. RESULTS

We studied three different $^{151}Eu^{3+}$ sites of different symmetry for which sufficient crystal-field and hyperfine data exists in the literature. These were the C_{4v} and C_{3v} sites in CaF_2, and the C_2 site in $EuCl_3 \cdot 6H_2O$. Table I lists the fitted crystal-field values for each site.

A. Eu^{3+}:CaF_2 C_{4v} center

In the C_{4v} site of CaF_2, Eu^{3+} substitutes for Ca^{2+}, with charge compensation arising from an interstitial neighboring F^- ion. There are values in the literature for the Zeeman-hyperfine splittings of the $^7F_0$ and $^5D_0$ states [55], the energy levels [56], and the fitted crystal-field parameters [56]. Here, we refitted the crystal-field parameters in the full model using the published experimental energy levels [56]. Fitted crystal-field parameters are given in Table I, and experimental and calculated spin Hamiltonian parameters given in Table II. The refitted crystal-field parameters are within ∼10% of the values given in Ref. [56]. This small change is expected as our fit gives equal weight to the Zeeman-hyperfine splittings, which are most strongly influenced by the positions of the crystal-field levels in the $^7F_1$ and $^7F_2$ multiplets. Figure 1 shows the comparison between experimental and fitted hyperfine structure for the $^7F_0$ and $^5D_0$ states. The Zeeman structure is displayed for fields in a circle in the xz plane:

$$\mathbf{B} = \begin{bmatrix} B_0 \cos(2\pi t) \\ B_0 \sin(2\pi t) \end{bmatrix}. \tag{35}$$

The C_{4v} site of CaF_2 is a good illustration of the established qualitative understanding of hyperfine structure in the $J = 0$ levels of Eu^{3+}, which we briefly summarize. The zero field

TABLE II. Spin Hamiltonian parameters for the $^{151}Eu^{3+}$:CaF_2C_{4v} site calculated from crystal-field fitting compared to experimental spin Hamiltonian parameters [55]. In that work, signs of the g-values could not be determined, so we list them with "$\pm$" here.

	$^7F_0$		$^5D_0$	
	Calc	Expt	Calc	Expt
D_{pq}(MHz)	0.198	–	0.00265	–
D_{4f}(MHz)	10.968	–	0.661	–
D_{lat}(MHz)	−13.562	–	−13.708	–
D_{tot}(MHz)	−2.395	−2.415	−13.045	−13.05
g_x(MHzT^{-1})	−0.936	±0.212	9.646	–
g_y(MHzT^{-1})	−0.936	±0.212	9.646	–
g_z(MHzT^{-1})	5.075	±4.657	9.761	–

hyperfine structure in these levels arises from the combination of the lattice quadrupole interaction and effects due to the admixture of $J = 2$ crystal-field levels into the $^7F_0$ and $^5D_0$ wave functions by the crystal field [24,57]. This mixing is only large in the ground state as the separation of the $J = 2$ levels (the $^7F_2$ multiplet) is much smaller than in the excited state (the $^5D_2$ multiplet). This is clear from the fitted wave functions of the $^7F_0$ and $^5D_0$ states (ignoring contributions <1%):

$$\Psi(^7F_0) = -0.99|^7F_0, 0\rangle + 0.12|^7F_2, 0\rangle, \tag{36}$$

$$\Psi(^5D_0) = +1.00|^5D_0, 0\rangle. \tag{37}$$

This mixing gives rise to the $4f$ contribution to the spin Hamiltonian quadrupole term, which is only significant in the $^7F_0$ state. However, since this term is of opposite sign to the lattice quadrupole term, the result is smaller quadrupole tensor in the $^7F_0$ state.
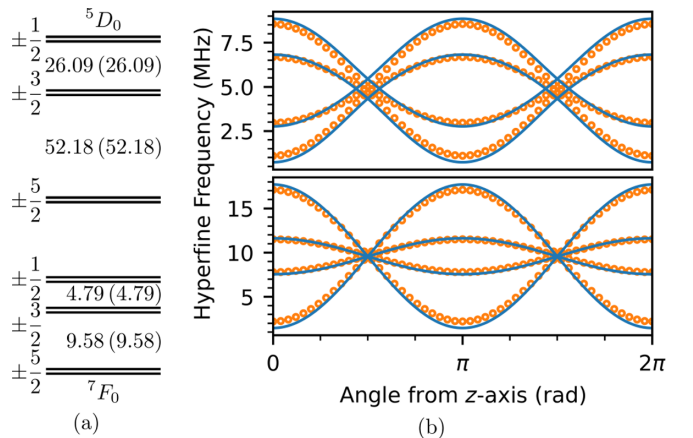

FIG. 1. (a) Calculated zero field splittings of the Eu^{3+}:CaF_2C_{4v} site with experimental splittings given in brackets. (b) Calculated (blue) and experimental (orange) Zeeman splittings of the $^7F_0$ $\pm\frac{3}{2} \rightarrow \pm\frac{1}{2}$ (top) and $\pm\frac{5}{2} \rightarrow \pm\frac{3}{2}$ (bottom) hyperfine transitions for a magnetic field of 400 mT rotated in the xz plane. Experimental points are calculated from published experimental spin Hamiltonian parameters [55].

For this C$_4$ site, Fig. 1(a) shows that the agreement between experimental and calculated zero field splittings is excellent. The quantitative parameter results (Table II) also agree well with the qualitative description above. In the $^5D_0$ state, the lattice contribution to the quadrupole term is over 95%, whereas in the ground state, roughly equal magnitude, opposite sign $4f$ and lattice contributions result in a quadrupole $<20\%$ of the excited state. In both states, the pseudoquadrupole contribution to the quadrupole tensor is near negligible. This term arises from interactions with $\Delta M_J = 0, 1$ levels. For $J \neq 0$ states, the pseudoquadrupole can be significant since these interactions exist within the multiplet. However, for the $J = 0$ levels, the large separations to the interacting $^7F_1$ and $^5D_1$ states largely suppress this term.

While the zero field structure of the $J = 0$ levels is determined by mixing with $J = 2$ multiplets, the Zeeman structure in a magnetic field is understood to be determined by the small amount of mixing with the $J = 1$ multiplets. This mixing allows for nonzero matrix elements for the electronic Zeeman interaction between the nuclear states [45]. While in $J \neq 0$ states this pseudonuclear Zeeman term typically entirely dominates the bare moment, the large spacing to the $J = 1$ multiplets means the contribution is much smaller for $J = 0$ states [24]. Again, the contribution is typically only significant in the $^7F_0$ state due to the smaller separation to $^7F_1$, and again, it is of similar size and opposite sign to that of the true nuclear Zeeman effect. This means g-values are typically smaller in the $^7F_0$ state compared to the $^5D_0$ state. Depending on the proximity of the $^7F_1$ levels, the pseudonuclear Zeeman contribution can be large enough that the sign of the g-values is reversed relative to the bare nuclear magnetic moment.

We see from Fig. 1(b) and Table II that, as expected, in $^5D_0$ the predicted g-values are only slightly reduced from the bare moment of 10.58 MHz T^{-1} by the small amount of mixing with $^5D_1$. In the ground state, the g values are substantially reduced by the mixing. The predicted values in this level do differ from the experimental numbers. This discrepancy can be attributed to the $\sim5\%$ deviation of the calculated crystal-field splittings of the $^7F_1$ from the experimental values, since the pseudonuclear term is highly sensitive to the separation of the $^7F_1$ and $^7F_0$ levels. Nevertheless, the agreement is sufficient to resolve the sign ambiguity in the experimental g values: $g_{x,y}$ is negative, and g_z is positive.

B. Eu^{3+}:CaF$_2$:O^{2-} C$_{3v}$ center

In the C$_{3v}$ site of CaF$_2$, denoted the G1 center, Eu^{3+} substitutes for Ca^{2+} with charge compensation arising from a substitutional O^{2-} in a neighboring F$^-$ site. Zeeman-hyperfine splittings for this site are available for both the $^7F_0$ ground and $^5D_0$ excited states [27,43,58–61], but despite these extensive hyperfine studies, the observed crystal-field levels are restricted to few ^7F_J and ^5D_J multiplets [27]. Fitting a set of crystal-field parameters to the available energy levels is further complicated by the very strong crystal field caused by the nearby oxygen atom [58] which makes assignment of the $^7F_1$ and $^7F_2$ levels difficult [27,58]. As there has been no prior crystal-field fits to the G1 center and the ordering of the $^7F_{1,2}$ levels is unknown, we estimated a set of initial crystal-field parameters by hand using the $^5D_1$ and

TABLE III. Spin Hamiltonian parameters for the ^{151}Eu^{3+}:CaF$_2$C$_{3v}$ site calculated from crystal-field fitting compared to experimental spin Hamiltonian parameters [61].

	$^7F_0$		$^5D_0$	
	Calc	Expt	Calc	Expt
D_{pq}(MHz)	0.610	–	0.00809	–
D_{4f}(MHz)	31.988	–	2.170	–
D_{lat}(MHz)	−24.344	–	−24.573	–
D_{tot}(MHz)	8.256	8.26	−22.395	−22.23
g_x(MHzT^{-1})	−9.658	−8.998	9.504	9.527
g_y(MHzT^{-1})	−9.658	−8.998	9.504	9.527
g_z(MHzT^{-1})	8.948	9.739	9.751	10.056

$^5D_2$ splittings. This set was then refined by fitting to all of the available crystal-field and Zeeman-hyperfine data for the site. The ordering of the $^7F_1$ and $^7F_2$ levels could then be inferred from the crystal-field calculation, demonstrating that the unusually large crystal field causes an overlap of the $^7F_1$ and $^7F_2$ multiplets. Fitted crystal-field parameters are given in Table I, and experimental and calculated spin Hamiltonian parameters given in Table III. Figure 2 demonstrates the very good agreement between fitted and experimental splittings, with Zeeman structure calculated using Eq. (35).

Unlike the C$_{4v}$ center, the C$_{3v}$ center does not conform well to the normal picture for $J = 0$ energy level structure because the unusually large crystal field causes considerable mixing between multiplets. In the $^5D_0$ state, the quadrupole interaction $D = -22.395$ MHz is still primarily due to the lattice quadrupole $D_{lat} = -24.573$ MHz, but the contribution from the $4f$ quadrupole $D_{4f} = 2.170$ MHz is double that for the C$_{4v}$ center. This is due to the large $B_0^2 = 2122$ cm^{-1} term mixing the $^5D_0$ with the $^5D_2$ state despite these multiplets being separated by ≈ 4000 cm^{-1}. The calculated wave functions

$$\Psi(^7F_0) = +0.92|^7F_0, 0\rangle - 0.35|^7F_2, 0\rangle + 0.11|^7F_4, 0\rangle$$
$$+ 0.10|^7F_4, -3\rangle - 0.10|^7F_4, 3\rangle, \tag{38}$$

$$\Psi(^5D_0) = -1.00|^5D_0, 0\rangle + 0.04|^5D_2, 0\rangle, \tag{39}$$

demonstrate the considerable mixing compared to the C$_{4v}$ site.

In the ^7F multiplet, the crystal-field splittings of the $^7F_1$ and the $^7F_2$ states generated by the B_0^2 and B_q^4 terms are so large that, as described above, the multiplets are no longer separated and the ordering of states is not obvious. In particular, a doublet state of $^7F_2$ at 758 cm^{-1} is lower in energy compared to the singlet state of $^7F_1$ at 865 cm^{-1} (see Table I in Ref. [39]). The low lying $^7F_2$ mixes strongly with $^7F_0$ resulting in a large $4f$ quadrupole contribution $D_{4f} = 31.988$ MHz. This is larger than the lattice quadrupole contribution $D_{lat} = -24.344$ MHz, resulting in a total quadrupole interaction of $D_{tot} = 8.256$ MHz. This reversal of the sign of the quadrupole interaction results in a reversal of the ordering of the nuclear spin states compared to the $^5D_0$ state.

The g values of the C$_{3v}$ site do follow a similar pattern to the C$_{4v}$ case. In the excited state, the g values are only slightly reduced from the bare moment with good agreement between calculation and experiment. Despite the strong crystal field,
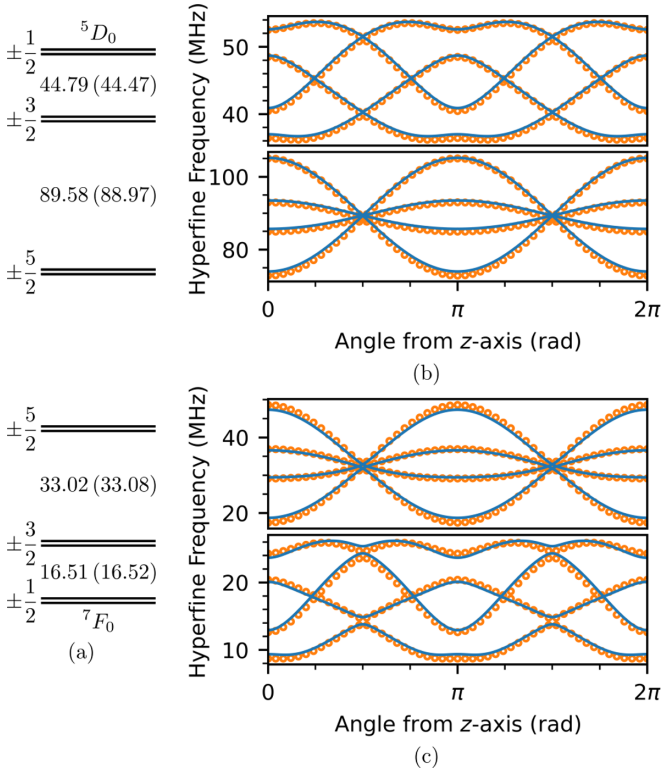
FIG. 2. (a) Calculated zero field splittings of the Eu^{3+}:CaF_2C_{3v} site with experimental splittings given in brackets. (b) Calculated (blue) and experimental (orange) Zeeman splittings of the $^5D_0 \pm\frac{3}{2} \rightarrow \pm\frac{1}{2}$ (top) and $\pm\frac{5}{2} \rightarrow \pm\frac{3}{2}$ (bottom) hyperfine transitions for a magnetic field of 400 mT rotated in the x-z plane. (c) Calculated (blue) and experimental (orange) Zeeman splittings of the $^7F_0 \pm\frac{3}{2} \rightarrow \pm\frac{5}{2}$ (top) and $\pm\frac{1}{2} \rightarrow \pm\frac{3}{2}$ (bottom) hyperfine transitions for a magnetic field of 400 mT rotated in the xz plane. Experimental points are calculated from published experimental spin Hamiltonian parameters [61].

the splittings between the $^5D_0$ and $^5D_1$ states are still large. The influence of the large crystal field is seen more strongly in the ground state. The large splitting within the $^7F_1$ state pushes the $M_J = \pm1$ doublet far closer to the $^7F_0$ state. The resulting large mixing via the magnetic dipole interaction results in a pseudonuclear Zeeman effect almost twice the size of the bare moment in the x and y directions. Conversely, since the $^7F_1$ singlet state is pushed up, the z component of the pseudonuclear Zeeman effect is small (<2 MHz T^{-1}) as it arises from mixing with this term. The result is $g_{x,y}$ and g_z values of similar magnitude but opposite sign, agreeing well with the experimental values. Differences in the calculated and experimental $^7F_0$ g-values are due to inaccuracies in the fitted crystal-field levels as the mixing of states is proportional to the splitting as evidenced in Eq. (24).

Previous works have attempted to explain the large pseudonuclear Zeeman contribution observed in $^7F_0$ of the C_{3v} center [27,61]. This was done without the use a crystal-field calculation and it was thought that J mixing of $^7F_2$ into $^7F_0$ would not exceed 1%. Based on this assumption it was concluded that J mixing could not explain the observed deviations of the electronic Zeeman and magnetic dipole matrix elements from their free-ion values. However, by performing a

TABLE IV. ^{151} $EuCl_3 \cdot 6H_2O$ spin Hamiltonian parameters calculated from crystal-field fitting compared to experimental spin Hamiltonian parameters [69]. Note that we have transformed the spin Hamiltonian parameters of Ref. [69] into the standard electron paramagnetic formalism: the zyz Euler rotation convention, Eq. (A1). Further, we have chosen the opposite set of equivalent spin Hamiltonian E, g_x and g_y parameters to match the crystal-field fit as described in the text.

	$^7F_0$		$^5D_0$	
	Calc	Expt	Calc	Expt
D_{pq} (MHz)	0.0550	–	0.000239	–
E_{pq} (MHz)	0.0938	–	0.000725	–
γ_{pq} (°)	−68.33	–	−68.33	–
D_{4f} (MHz)	2.109	–	0.0497	–
E_{4f} (MHz)	4.275	–	0.199	–
γ_{4f} (°)	−68.01	–	−68.01	–
D_{lat} (MHz)	−1.866	–	−1.875	–
E_{lat} (MHz)	9.263	–	9.284	–
γ_{lat} (°)	12.89	–	12.89	–
D_{tot} (MHz)	0.29718	0.35692	−1.82529	−1.85868
E_{tot} (MHz)	5.29024	5.29026	9.08941	9.08595
γ_{Qtot} (°)	5.43	2.93	12.76	13.22
g_x (MHzT^{-1})	4.115	±4.029	9.690	9.666
g_y (MHzT^{-1})	−1.723	∓1.504	9.647	9.293
g_z (MHzT^{-1})	2.857	3.006	9.686	10.025
γ_M (°)	21.81	22.69	19.30	3.1

complete crystal-field calculation, we have been able to show that J mixing is far larger than previously thought, close to 13%, which is sufficient to explain the observed pseudonuclear Zeeman effect.

C. EuCl$_3 \cdot$ 6H$_2$O C$_2$ center

$EuCl_3 \cdot 6H_2O$ is a stoichiometric crystal in which the Eu^{3+} ion occupies a single site of C_2 symmetry. Several papers over many years have studied the electronic and Zeeman-hyperfine structure [62–68], and it has more recently been investigated for quantum information applications [69–71].

The nonaxial site symmetry means that additional crystal-field terms must be included: 15 crystal-field parameters compared to the 5 (6) for the C_{4v} (C_{3v}) sites. The large number of crystal-field parameters caused previous workers to fit the $EuCl_3 \cdot 6H_2O$ crystal field in the higher C_{2v} symmetry [63], but it is precisely the additional crystal-field terms that generate the correctly shaped spin Hamiltonian quadrupole and Zeeman tensors. The quadrupole and Zeeman tensors arising from each of the interactions described in Sec. III B are no longer axial, and the principal axes of these tensors need only coincide along the C_2 direction. Here, we use a selection of the energy levels from Ref. [63] along with some new ^7F_J levels determined from fluorescence measurements to fit the site (see Table I in Ref. [39]) using C_2 symmetry and the method described in Sec. IV. Fitted crystal-field parameters are given in Table I, and experimental and calculated spin Hamiltonian parameters given in Table IV. The fitted crystal-field parameters are notably different to the those of Ref. [63]. This is due to a combination of the lowering of symmetry from
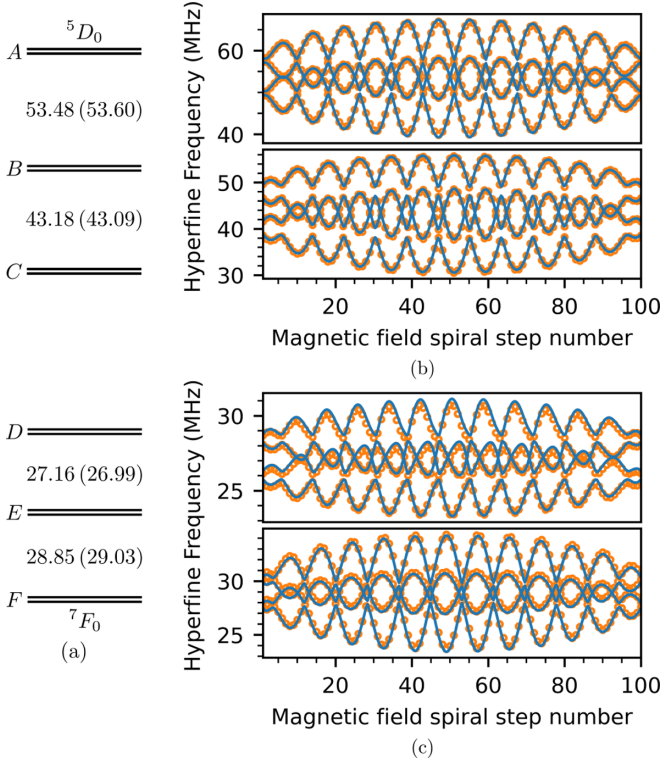
FIG. 3. (a) Calculated zero field splittings of the $EuCl_3 \cdot 6H_2OC_2$ site with experimental splittings given in brackets. (b) Calculated (blue) and experimental (orange) Zeeman splittings of the $^5D_0$ $B \to A$ (top) and $C \to B$ (bottom) hyperfine transitions for a magnetic field spiral of 400 mT. (c) Calculated (blue) and experimental (orange) Zeeman splittings of the $^7F_0$ $E \to D$ (top) and $F \to E$ (bottom) hyperfine transitions for a magnetic field spiral of 400 mT. Experimental points are calculated from published experimental spin Hamiltonian parameters [69].

C_{2v} to C_2 and the use of different fixed free-ion parameters. Despite the low symmetry, the agreement between experimental and calculated hyperfine splittings is excellent, as shown in Fig. 3. To display the Zeeman splitting in this nonaxial site, we have calculated the structure for the magnetic field spiral in Eq. (34).

Again, the excited state quadrupole is dominated by the lattice term, where the additional parameter E accounts for the asymmetry of this nonaxial site. The calculated wave functions

$$\Psi(^7F_0) = (-0.11 - 0.99i)|^7F_0, 0\rangle + (0.05 + 0.04i)|^7F_2, 2\rangle$$
$$+ (-0.04 + 0.05i)|^7F_2, -2\rangle, \quad (40)$$

$$\Psi(^5D_0) = (-0.34 - 0.94i)|^5D_0, 0\rangle, \quad (41)$$

show the strong mixing of the $M_J = \pm 2$ $^7F_2$ levels into $^7F_0$ due to the large B_2^2 crystal-field parameter. Similarly, there is no mixing of the $M_J = 0$ $^7F_2$ level into $^7F_0$ by the much weaker B_0^2 crystal-field parameter. As the rank two crystal-field parameters are directly related to D and E, this explains the large asymmetry of the spin Hamiltonian quadrupole contributions. There is close agreement between the experimental and calculated values for both the principal axes values and

orientation of the tensor. The ground state has comparable $4f$ and lattice quadrupole contributions. These two terms have different orientations of the principle axes, leading to the overall quadrupole tensor in the ground state being misaligned from the excited state by $10°$, in reproducing the rotation seen in the experimental data. The fit also resolved the ambiguity in the sign of E: as described in Sec. III B, in a C_2 site the sign of E is poorly defined in a spin Hamiltonian model because a reversal of sign can be compensated for by rotating the M tensor to redefine the orientation of the x and y axes. However, the sign of E has physical significance in the crystal-field model, and the fit shows that, indeed, the sign of E is negative and the experimental spin Hamiltonian parameters need to be transformed $E \to -E$, $(g_x, g_y) \to (g_y, g_x)$, $\gamma \to \gamma \pm 90°$.

The excited state g values are again, only slightly reduced from the bare moment. The larger, $10°$, discrepancy with the experimental orientation of the Zeeman tensor is unsurprising: given the tensor is nearly isotropic, its orientation is not well defined in either the experimental data or the theoretical calculation. In the ground state, the agreement between experimental data and calculation is close, with the nonaxial symmetry giving rise to three unique g values. From the point of view of the crystal field, this occurs because the additional crystal-field parameters split the $M_J = \pm 1$ doublet. The matrix elements of $L_x + 2S_x$ and N_x are large between $^7F_0$ and the $M_J = +1$ singlet of $^7F_1$, and the matrix elements of $L_y + 2S_y$ and N_y are large between $^7F_0$ and the $M_J = -1$ singlet of $^7F_1$. As the $M_J = -1$ singlet is the lowest lying $^7F_1$ state with a gap of 301 cm^{-1}, the pseudonuclear contribution is largest for fields applied in the y direction, resulting in a large negative contribution to the g value, sufficient to reverse the sign of the term. Similarly, the smaller x contribution from the $M_J = +1$ singlet 428 cm^{-1} away results in a g_x value closer to the bare moment, with g_z taking a value between these two extremes. Previous work [69] was only able to determine that g_x and g_y had opposite signs; this fit resolves this sign ambiguity.

The Zeeman-hyperfine splittings were also calculated for $^{153}Eu^{3+}$ by scaling the hyperfine and nuclear Zeeman parameters by the ratio $^{153}Eu / ^{151}Eu$ of the electric quadrupole moment Q ($Q(^{153}Eu) = 2.412$ b and $Q(^{151}Eu) = 0.903$ b [72]) and nuclear magnetic moment g_n ($g_n(^{153}Eu) = 1.5330$ and $g_n(^{151}Eu) = 3.4717$ [73]). This is not sufficient to match the experimental hyperfine structure, since there is an isotope shift in the crystal-field levels which slightly $\mathcal{O}(1\%)$ alters the electronic contributions to the hyperfine levels. This shift is ~ 220 MHz on the $^7F_0 \to {}^5D_0$ transition but can be expected to be much larger on $J \neq 0$ transitions. To account for these differences, we fine-tuned the full set of crystal-field parameters to obtain the fitted values in Table V.

Relative oscillator strengths between $^7F_0$ and $^5D_0$ may be calculated using Eq. (21) (Table VI), or the equivalent expression for the full crystal-field Hamiltonian. Since both electronic states are singlets, the relative intensities are determined by the overlap of the nuclear spin states between the ground and excited states. This calculation provides an independent test of the model with data that was not used in the fitting process. Since experimental oscillator strengths are not directly available, we instead compared the excitation spectrum these values generate for the $^7F_0 \to {}^5D_0$ transition with the experimental spectrum for $Eu^{35}Cl_3 \cdot 6H_2O$ in Fig. 4.

TABLE V. ^{153}EuCl$_3 \cdot$ 6H$_2$O spin Hamiltonian parameters calculated from crystal-field fitting compared to experimental spin Hamiltonian parameters [69]. Note that we have transformed the spin Hamiltonian parameters of Ref. [69] into the standard electron paramagnetic formalism: the *zyz* Euler rotation convention, Eq. (A1). Further, we have chosen the opposite set of equivalent spin Hamiltonian E, g_x and g_y parameters to match the crystal-field fit as described in the text.

	$^7F_0$		$^5D_0$	
	Calc	Expt	Calc	Expt
D_{tot}(MHz)	0.813097	0.791815	−4.815367	−4.80
E_{tot}(MHz)	13.648917	13.660932	23.209892	23.21
$\gamma_{Qt\alpha}(^\circ)$	3.21	2.93	12.19	13.22
g_x(MHzT^{-1})	1.878	±1.794	4.315	4.269
g_y(MHzT^{-1})	−0.422	∓0.673	4.298	4.105
g_z(MHzT^{-1})	1.381	1.359	4.315	4.428
γ_M $(^\circ)$	23.08	22.69	20.47	3.1

The simulated spectrum has only three free parameters: the overall amplitude, the isotope shift (which is too small to be accurately reproduced by the crystal-field model), and a parameter accounting for absorption. Given this, the very good agreement confirms the calculated oscillator strengths are accurate.

VI. DISCUSSION

We have shown crystal-field theory can be used to accurately calculate Zeeman-hyperfine splittings of the $J = 0$ levels in several different Eu^{3+} impurity centers as long as the nuclear Zeeman and lattice electric quadrupole terms are included in the calculation. In particular, the lattice contribution to the nuclear quadrupole energy can be accurately calculated as shown by the $^5D_0$ splittings in each material, including calculating the rotation about the symmetry axis (in low symmetry) for both the lattice and $4f$ contributions. The crystal-field mixing of the $^7F_2$ and $^7F_1$ levels into $^7F_0$ is also well reproduced, allowing accurate determination of the

TABLE VI. Oscillator strengths of the EuCl$_3 \cdot$ 6H$_2$O $^7F_0 \to {}^5D_0$ nuclear state transitions. State labels follow those of Fig. 3. Calculated values are given by the overlap of the crystal-field nuclear wave functions and experimental values are taken from [69].

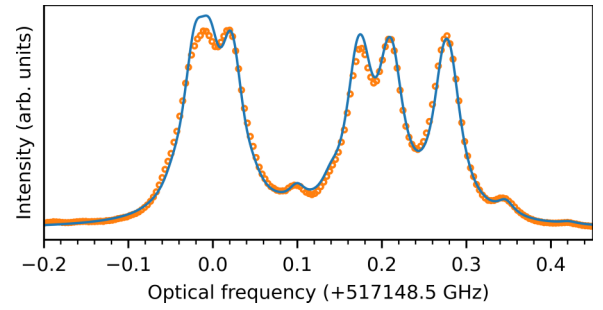|	^{151}Eu^{3+}		^{153}Eu^{3+}	
	Calc	Expt	Calc	Expt
$F \to C$	0.9608	0.9300	0.9446	0.9302
$F \to B$	0.0341	0.0608	0.0483	0.0609
$F \to A$	0.0050	0.0091	0.0071	0.0089
$E \to C$	0.0378	0.0687	0.0541	0.0686
$E \to B$	0.9322	0.8766	0.9031	0.8771
$E \to A$	0.0299	0.0547	0.0428	0.0544
$D \to C$	0.0013	0.0013	0.0013	0.0013
$D \to B$	0.0336	0.0626	0.0486	0.0620
$D \to A$	0.9650	0.9362	0.9501	0.9367

FIG. 4. Simulated and experimental spectra of the $^7F_0 \to {}^5D_0$ nuclear state transitions of ^{151}Eu^{3+} and ^{153}Eu^{3+} in EuCl$_3 \cdot$ 6H$_2$O. Simulated spectra were calculated using the function $\Gamma(f) = A_0\alpha(f)e^{-\alpha(f)A_1}$ which accounts for absorption of the light in this optically thick sample before reaching the point in the crystal from which emission was collected. We used a Lorentzian line shape α with FWHM line width 0.0122 GHz and an ^{153}Eu^{3+} transition offset of 0.220 GHz.

hyperfine structure of this state. In the C$_{3v}$ case, we showed that the large deviation of the magnetic dipole and electronic Zeeman matrix elements from their free-ion values [61] is indeed due to an extraordinarily large J mixing of the $^7F_2$ and $^7F_4$ levels into $^7F_0$, resolving an open question in the literature.

The model fit the hyperfine structure of each material remarkably well despite, in some cases, how few crystal-field levels were available to constrain the fits. In fact, this is the result of a unusual property of the low lying levels in Eu^{3+}: certain crystal-field levels have reduced matrix elements $\langle\Psi||U^{(k)}||\Psi\rangle$ which are large for particular k-values and small or near-zero for all other k, allowing those levels to be used to constrain the corresponding crystal-field parameter. In Eu^{3+}, $^7F_1$ is sensitive to B_q^2, $^7F_2$ is sensitive to B_q^4, and $^7F_3 / {}^7F_4$ are sensitive to B_q^6, along with $^5L_6$ to a lesser extent. Whilst there are similar relationships between parameters and individual multiplets and crystal-field parameters in other ions (see Ref. [38] for a full list), Eu^{3+} is particular as these special levels are low-lying, so are readily observed in fluorescence spectra of the $^5D_0$ level. Further, their assignment is rarely ambiguous due to the true singlet nature of $^7F_0$ and $^5D_0$ levels, and the large separations ^7F_J and ^5D_J levels. It is only in particularly unusual cases such as the CaF$_2$C$_{3v}$ site that ^7F multiplets overlap. For these reasons, Eu^{3+} might be a good dopant choice when trying to work out the crystal-field fitting parameters of a new host material: since parameters vary only slowly across the rare-earth series [31] parameters from Eu^{3+} could be used as an initial guess for other rare-earth dopants for which assigning observed energy levels is more difficult.

We have emphasized, and demonstrated, that crystal-field fits can resolve spin Hamiltonian ambiguities. However, this requires considerable care to be taken during the fitting process, because there are ambiguities in the crystal-field fit itself when fitting to only the energies of crystal-field levels. There are two types of ambiguity that manifest in crystal-field fitting [74,75]. The first are rotations of the crystal-field parameters about the symmetry axis, which occur in centers with imaginary components. The rotational ambiguity arises when the

relationship between the crystal field and the experimental crystallographic axes is unknown. It is only by constraining the crystal-field parameters through measurements that depend on the true orientation of the crystal, such as Zeeman splittings, that we can resolve this ambiguity. The second ambiguity is complete re-orientations of the symmetry axis which can yield as many as six numerically equivalent crystal-field parameter sets [75]. This is typically only an issue at orthorhombic and lower symmetries [74,76] with multiple nonzero crystal-field parameters of every rank. Whilst the calculated splittings are equivalent for these different sets, the calculated wave functions will differ. Therefore it is possible to determine the correct set of crystal-field parameters by comparing wave function dependent quantities, such as oscillator strengths and Zeeman splittings, to experimental values.

In Eu^{3+}, wave function-dependent information can be obtained with relative ease. This includes the ordering of the $^7F_1$ M_J levels, and the ordering of the $^5D_0$ M_I hyperfine states at zero-field. In high symmetry where the only nonzero rank two crystal-field parameter is B_0^2, the $^5D_0$ hyperfine state ordering is sufficient due to the relationship between the splittings and the lattice quadrupole [Eq. (16)]. However, in lower symmetry the introduction of additional B_q^2 parameters means there is insufficient information from just this ordering, and knowledge of the ordering of the $^7F_1$ levels is needed as well. This can be achieved by measuring the polarized absorption or fluorescence of the $^7F_1 \longleftrightarrow {}^5D_0$ transition, or by measuring the $^7F_0$ nuclear Zeeman g values. Once the ordering of the $^7F_1$ levels is known, these can be used to determine the sign and magnitudes of B_q^2 as there is a straightforward relationship between the ordering of the states and the parameters [38]. Restricting the rank two parameters to a single set then restricts the other crystal-field parameters. Solving the crystal-field parameters sets ambiguities simultaneously solves the spin Hamiltonian sign ambiguities.

Comparison of the experimental and calculated crystal-field highlights a well-known limitation of the standard, one-electron crystal-field model used here: the model omits two-electron perturbation correlation effects (referred to as the correlation crystal field) [38]. These additional effects are known to be important for correctly predicting orderings and splittings of the ^5D_J states of Eu^{3+}[77], and, indeed, we see larger deviations between experimental and calculated parameters for those levels (Table I of Ref. [39]). Additionally, omitting these effects can cause a change in the free-ion parameters F_k, artificially pushing the ^7F_J states down in energy. This is the likely source of the discrepancies of the calculated $^7F_0$ and $^7F_1$ levels in $EuCl_3 \cdot 6H_2O$, with each shifted downward by significantly more than the standard deviation $\sigma = 15\,cm^{-1}$. It is not normally practical to include the correlation crystal field because doing so requires a large number of additional parameters, up to 637 for the lowest site symmetry

[78]. Therefore effects that would otherwise be accounted for by the correlation crystal field are instead absorbed by the single-electron crystal field. This results in crystal-field parameters that are not necessarily a true representation of the crystal-field potential.

We made one modification to the model to minimize the effect of this small distortion of the crystal-field parameters. Eq. (16) shows that the lattice electric quadrupole N_q^2 parameters should have a fixed dependence on the single-electron crystal-field B_q^2 parameters. Instead, we allowed the lattice quadrupole parameters N_q^2 to vary semi-independently of B_q^2, which avoids propagating the distortion of the crystal-field parameters through to the hyperfine structure. In this way, the N_q^2 parameters are more representative of the true crystal field than the B_q^2 parameters. This ensures a satisfactory fit to both the hyperfine and crystal-field structure, whilst maintaining consistency between the crystal-field and quadrupole parameters.

VII. CONCLUSIONS

We have calculated Zeeman-hyperfine splittings of Eu^{3+}in three crystallographic centers, the C_{4v} and C_{3v} sites of CaF_2as well as the C_2 site of $EuCl_3 \cdot 6H_2O$, using a complete crystal-field model, with excellent agreement between experimental and calculated values. This was achieved by including the lattice quadrupole interaction and nuclear Zeeman interaction in the complete crystal-field calculation; an important step for accurate calculations of hyperfine splittings for non-Kramers singlet states. We have also demonstrated accurate crystal-field calculations of oscillator strengths in low symmetry (C_2) by using all parameters required for the exact symmetry of the site.

ACKNOWLEDGMENTS

APPENDIX

The *zyz* Euler rotation convention used is given by

$$R(\varphi, \theta, \psi) = \begin{bmatrix} \cos\varphi & \sin\varphi & 0 \\ -\sin\varphi & \cos\varphi & 0 \\ 0 & 0 & 1 \end{bmatrix} \times \begin{bmatrix} \cos\theta & 0 & -\sin\theta \\ 0 & 1 & 0 \\ \sin\theta & 0 & \cos\theta \end{bmatrix}$$
$$\times \begin{bmatrix} \cos\psi & \sin\psi & 0 \\ -\sin\psi & \cos\psi & 0 \\ 0 & 0 & 1 \end{bmatrix}. \tag{A1}$$

[1] G. Hétet, J. J. Longdell, M. J. Sellars, P. K. Lam, and B. C. Buchler, Phys. Rev. Lett. **101**, 203601 (2008).

[2] M. Afzelius, C. Simon, H. de Riedmatten, and N. Gisin, Phys. Rev. A **79**, 052329 (2009).

[3] E. Fraval, M. J. Sellars, and J. J. Longdell, Phys. Rev. Lett. **92**, 077601 (2004).

[4] O. Guillot-Noël, P. Goldner, E. Antic-Fidancev, and J. L. Le Gouët, Phys. Rev. B **71**, 174409 (2005).

[5] O. Guillot-Noël, Y. Le Du, F. Beaudoux, E. Antic-Fidancev, M. F. Reid, R. Marino, J. Lejay, A. Ferrier, and P. Goldner, J. Lumin. **130**, 1557 (2010).

[6] M. Zhong, M. P. Hedges, R. L. Ahlefeldt, J. G. Bartholomew, S. E. Beavan, S. M. Wittig, J. J. Longdell, and M. J. Sellars, Nature (London) **517**, 177 (2015).

[7] D. P. McLeod and M. F. Reid, J. Alloys Compd. **250**, 302 (1997).

[8] Jon-Paul R. Wells, G. D. Jones, and R. J. Reeves, Phys. Rev. B **60**, 851 (1999).

[9] P. Goldner and O. Guillot-Noël, Mol. Phys. **102**, 1185 (2004).

[10] P. Goldner and O. Guillot-Noël, J. Alloys Compd. **451**, 682 (2008).

[11] M. N. Popova, E. P. Chukalina, B. Z. Malkin, and S. K. Saikin, Phys. Rev. B **61**, 7421 (2000).

[12] K. I. Gerasimov, M. M. Minnegaliev, B. Z. Malkin, E. I. Baibekov, and S. A. Moiseev, Phys. Rev. B **94**, 054429 (2016).

[13] S. P. Horvath, J. V. Rakonjac, Y. H. Chen, J. J. Longdell, P. Goldner, J. P. R. Wells, and M. F. Reid, Phys. Rev. Lett. **123**, 057401 (2019).

[14] M. N. Popova, S. A. Klimin, S. A. Moiseev, K. I. Gerasimov, M. M. Minnegaliev, E. I. Baibekov, G. S. Shakurov, M. Bettinelli, and M. C. Chou, Phys. Rev. B **99**, 235151 (2019).

[15] J. P. R. Wells, G. D. Jones, M. F. Reid, M. N. Popova, and E. P. Chukalina, Mol. Phys. **102**, 1367 (2004).

[16] A. Baraldi, R. Capelletti, M. Mazzera, N. Magnani, I. Földvári, and E. Beregi, Phys. Rev. B **76**, 165130 (2007).

[17] M. Mazzera, R. Capelletti, A. Baraldi, E. Buffagni, N. Magnani, and M. Bettinelli, J. Phys.: Condens. Matter **24**, 205501 (2012).

[18] D. S. Pytalev, E. P. Chukalina, M. N. Popova, G. S. Shakurov, B. Z. Malkin, and S. L. Korableva, Phys. Rev. B **86**, 115124 (2012).

[19] G. S. Shakurov, E. P. Chukalina, M. N. Popova, B. Z. Malkin, and A. M. Tkachuk, Phys. Chem. Chem. Phys. **16**, 24727 (2014).

[20] K. N. Boldyrev, M. N. Popova, B. Z. Malkin, and N. M. Abishev, Phys. Rev. B **99**, 041105(R) (2019).

[21] S. Mothkuri, M. F. Reid, Jon-Paul R. Wells, E. Lafitte-Houssat, P. Goldner, and A. Ferrier, Phys. Rev. B **103**, 104109 (2021).

[22] G. K. Liu, J. Huang, R. L. Cone, and B. Jacquier, Phys. Rev. B **38**, 11061 (1988).

[23] Jon-Paul R. Wells and G. D. Jones, Phys. Rev. B **80**, 115105 (2009).

[24] R. J. Elliott, Proceedings of the Physical Society. Section B **70**, 119 (1957).

[25] R. M. Sternheimer, Phys. Rev. **146**, 140 (1966).

[26] J. Blok and D. A. Shirley, Phys. Rev. **143**, 278 (1966).

[27] A. J. Silversmith, High resolution laser spectroscopy of trivalent europium centers in crystals, Ph.D. thesis, Australian National University, 1985.

[28] B. G. Wybourne, *Spectroscopic Properties of Rare Earths* (Interscience, New York, 1965).

[29] M. Weissbluth, *Atoms and Molecules* (Academic Press, New York, 1978).

[30] G. Liu, in *Spectroscopic Properties of Rare Earths in Optical Materials*, edited by G. Liu and B. Jacquier (Springer, Berlin, 2005), Chap. 1, pp. 1–94.

[31] W. T. Carnall, G. L. Goodman, K. Rajnak, and R. S. Rana, J. Chem. Phys. **90**, 3443 (1989).

[32] K. Rajnak and B. G. Wybourne, Phys. Rev. **132**, 280 (1963).

[33] B. R. Judd, *Operator Techniques in Atomic Spectroscopy* (Princeton University Press, Princeton, NJ, 1998).

[34] B. R. Judd, Phys. Rev. **141**, 4 (1966).

[35] H. H. Marvin, Phys. Rev. **71**, 102 (1947).

[36] B. R. Judd, H. M. Crosswhite, and H. Crosswhite, Phys. Rev. **169**, 130 (1968).

[37] C. W. Nielson and G. F. Koster, *Spectroscopic Coefficients for the* p^n, d^n, *and* f^n *Configurations* (M. I. T. Press, Cambridge, Massachusetts, 1963).

[38] C. Görller-Walrand and K. Binnemans, in *Handbook on the Physics and Chemistry of Rare Earths*, Vol. 23 (Elsevier, Oxford, 1996), Chap. 155, pp. 121–283.

[39] See Supplemental Material at http://link.aps.org/supplemental/10.1103/PhysRevB.105.125141 for tables of the calculated crystal-field levels, mean free-ion parameters for trivalent europium, and symmetry restrictions on nonzero crystal-field parameters.

[40] D. J. Newman and B. Ng, Rep. Prog. Phys. **52**, 699 (1989).

[41] R. M. Sternheimer, Phys. Rev. **164**, 10 (1967).

[42] R. M. Sternheimer, Zeitschrift fur Naturforschung - Section A Journal of Physical Sciences **41**, 24 (1986).

[43] A. P. Radliński and A. J. Silversmith, Phys. Rev. B **34**, 86 (1986).

[44] M. Lovrić, P. Glasenapp, D. Suter, B. Tumino, A. Ferrier, P. Goldner, M. Sabooni, L. Rippe, and S. Kröll, Phys. Rev. B **84**, 104417 (2011).

[45] B. Bleaney, Physica **69**, 317 (1973).

[46] M. A. Teplov, Zh. Eksp. Teor. Fiz. 53, 1510 (1967) [Sov. Phys. JETP **26**, 872 (1968)].

[47] M. Lovrić, P. Glasenapp, and D. Suter, Phys. Rev. B: Condens. Matter Mater. Phys. **85**, 014429 (2012).

[48] N. L. Jobbitt, J. P. R. Wells, M. F. Reid, S. P. Horvath, P. Goldner, and A. Ferrier, Phys. Rev. B **104**, 155121 (2021).

[49] M. F. Reid, C.-K. Duan, and H. Zhou, J. Alloys Compd. **488**, 591 (2009).

[50] R. Macfarlane and R. Shelby, in *Spectroscopy of Solids Containing Rare Earth Ions* (Elsevier, Amsterdam, The Netherlands, 1987), Vol. 21, pp. 51–184.

[51] S. Horvath, High-resolution spectroscopy and novel crystal-field methods for rare-earth based quantum information processing, Ph.D. thesis, University of Canterbury, 2016.

[52] W. T. Carnall, H. Crosswhite, H. M. Crosswhite, and J. G. Conway, J. Chem. Phys. **64**, 3582 (1976).

[53] D. J. Wales and J. P. K. Doye, J. Phys. Chem. A **101**, 5111 (1997).

[54] D. J. Wales, Science **285**, 1368 (1999).

[55] A. J. Silversmith and R. M. MacFarlane, Phys. Rev. B **45**, 5811 (1992).

[56] Jon-Paul R. Wells and R. J. Reeves, Phys. Rev. B **64**, 035102 (2001).

[57] R. M. Shelby and R. M. MacFarlane, Phys. Rev. Lett. **47**, 1172 (1981).

[58] A. J. Silversmith and A. P. Radliński, J. Phys. C **18**, 4385 (1985).

[59] A. J. Silversmith and N. B. Manson, Phys. Rev. B **34**, 4854 (1986).

[60] A. J. Silversmith, A. P. Radlinski, and N. B. Manson, Le Journal de Physique Colloques **46**, C7-531 (1985).

[61] A. J. Silversmith, A. P. Radliński, and N. B. Manson, Phys. Rev. B **34**, 7554 (1986).

[62] J. J. Longdell, A. L. Alexander, and M. J. Sellars, Phys. Rev. B **74**, 195101 (2006).

[63] K. Binnemans and C. Görller-Walrand, J. Alloys Compd. **250**, 326 (1997).

[64] N. A. Stump, R. G. Haire, and J. R. Peterson, Spectrosc. Lett. **32**, 737 (1999).

[65] N. A. Stump, G. K. Schweitzer, J. K. Gibson, R. G. Haire, and J. R. Peterson, Appl. Spectrosc. **48**, 937 (1994).

[66] K. H. Hellwege and H. G. Kahle, Z. Phys. **129**, 62 (1951).

[67] H. G. Kahle, Z. Phys. **155**, 145 (1959).

[68] J. Martin, M. Sellars, P. Tuthill, N. Manson, G. Pryde, and T. Dyke, J. Lumin. **78**, 19 (1998).

[69] R. Ahlefeldt, Evaluation of a stoichiometric rare earth crystal for quantum computing, Ph.D. thesis, Australian National University, 2013.

[70] R. L. Ahlefeldt, D. L. McAuslan, J. J. Longdell, N. B. Manson, and M. J. Sellars, Phys. Rev. Lett. **111**, 240501 (2013).

[71] R. L. Ahlefeldt, M. J. Pearce, M. R. Hush, and M. J. Sellars, Phys. Rev. A **101**, 012309 (2020).

[72] Y. Tanaka, R. M. Steffen, E. B. Shera, W. Reuter, M. V. Hoehn, and J. D. Zumbro, Phys. Rev. C **29**, 1830 (1984).

[73] N. J. Stone, At. Data Nucl. Data Tables **90**, 75 (2005).

[74] C. Rudowicz and R. Bramley, J. Chem. Phys. **83**, 5192 (1985).

[75] C. Rudowicz, M. Chua, and M. Reid, Phys. B: Condens. Matter **291**, 327 (2000).

[76] C. Rudowicz, J. Chem. Phys. **84**, 5045 (1986).

[77] O. K. Moune and P. Caro, J. Less-Common Met. **148**, 181 (1989).

[78] D. Garcia and M. Faucher, in *Handbook on the Physics and Chemistry of Rare Earths* (Elsevier, Amsterdam, The Netherlands, 1995), Vol. 21, Chap. 144, pp. 263–304.